Science Advances
AAAS

Supplementary Materials for

A stretchable and strain-unperturbed pressure sensor for motion interference–free tactile monitoring on skins

Qi Su, Qiang Zou, Yang Li, Yuzhen Chen, Shan-Yuan Teng, Jane T. Kelleher, Romain Nith, Ping Cheng, Nan Li, Wei Liu, Shilei Dai, Youdi Liu, Alex Mazursky, Jie Xu, Lihua Jin, Pedro Lopes, Sihong Wang*

*Corresponding author. Email: sihongwang@uchicago.edu

Published 24 November 2021, *Sci. Adv.* **7**, eabi4563 (2021)
DOI: 10.1126/sciadv.abi4563

The PDF file includes:

Other Supplementary Material for this manuscript includes the following:

Supplementary Text

Text S1. Finite-element simulation for the mechanical behavior of the sensor.

We performed Finite-element (FE) simulations using ABAQUS/Standard for the strain-unperturbed pressure sensor, with the model including electrodes and their substrates, stiffening micro-electrodes, and the dielectric layer (fig. S1). All the components have the same dimensions as in the real sensor. We only simulated a unit cell, which is the smallest repeating geometric unit, under the in-plane strain (X-Y plane) condition. We defined periodic boundary conditions on its two vertical edges as

$$u_x^{\mathrm{r}} - u_x^{\mathrm{l}} = \varepsilon\left(X^{\mathrm{r}} - X^{\mathrm{l}}\right), u_y^{\mathrm{r}} - u_y^{\mathrm{l}} = 0,$$

where the ε represents the applied tensile strain, u_x and u_y denote the displacements in the x and y directions, respectively, the superscripts r and l denote the quantities related to the nodes on the right and left edges. For the simplicity of simulation, we assume that all the layers are completely bonded and there is no separation/delamination between materials. A surface-to-surface frictionless contact between the top electrode and the dielectric layer is defined.

We used a free mesh with triangular elements for all the regions. We seeded at least five nodes on the smallest features of the geometry. In the areas where the pyramids contact with the top electrode, the mesh is locally refined (100 nodes) such that the relation between the contact areas and applied pressure can be well captured. The element type is a second-order triangular (6-node) plane-strain modified hybrid element (CEP6MH in ABAQUS). All the polymer layers except the top electrode and its substrate are modeled as an incompressible Neo-Hookean material, with the initial shear moduli 0.1 MPa for the bottom electrode and its substrate, 333 MPa for the stiffening micro-electrodes, and 1 MPa for the dielectric layer. The top electrode and its substrate are modeled as a rigid line, since the top electrode is quite thin and its deformation in the vertical direction is limited.

The simulations contain two steps. The first step is to stretch the pressure sensor by applying a tensile strain ε ($0 \leq \varepsilon \leq 0.5$) in the horizontal direction. After the sensor is stretched, a vertical pressure is applied onto the top layer. The relations between the applied pressure and the contact area can then be obtained.

Text S2. Crosslinking mechanism of PVDF-HFP and HMDA.

The crosslinking mechanism is shown in Fig. S7. First, the vinylidene fluoride units of the PVDF-HFP chains create double bonds by eliminating HF under the action of alkaline HMDA. Then, the HMDA adds onto two CF=CH unsaturated backbones by Michael addition and forms C=N double bonds, creating bridges among the PVDF-HFP chains. Through increased density of bridges, the elasticity is largely enhanced.

Text S3. Finite-element simulation on different interspace distances of adjacent pyramids.

The simulations were carried out for varied interspace distances of adjacent pyramids (fig. S13) and the sensor with a smaller interspace distance showed lower sensitivity because of its higher density of pyramids. The sensor with a smaller interspace distance (1.55 mm) only can be stretched up to 25% due to the severe element distortions around the stiffening pixel. Furthermore, the strain-insensitivity is independent of the interspace distance of adjacent pyramids.

Text S4. Discussion on the reference sensors.

The adhesive layer, modulus of the top electrode substrate, and thickness of the top electrode substrate play important roles in the strain-unperturbed sensing performance.

The dielectric layer of the sensor without the adhesive layer (fig. S16) wrinkles upon stretching due to the dielectric layer's non-homogeneous Young's modulus. The wrinkling increases the contact area between the top electrode and dielectric layer so that the capacitance response at 50% strain is higher than that at 0% strain; this effect is especially prominent when the pressure is larger than 4 kPa.

The tensile stress of the PDMS electrode substrate is much larger than that of the Ecoflex one (fig. S17), therefore more applied pressure is counteracted by the tensile stress within the PDMS top electrode substrate. In the lower pressure range (i.e., 0 - 2 kPa), the sensor with the PDMS top electrode shows lower capacitance responses because of this effect. When the pressure is larger than 2 kPa, this effect becomes weaker, giving rise to overall similar capacitance responses.

When pressure is applied on the top electrode, not only do the pyramids undergo deformation, but also the top electrode has a "coverage effect" on the tips of pyramids (fig. S18). The "coverage effect" mainly depends on the thickness of the top-electrode's substrate. Therefore, the sensor with a thicker top-electrode's substrate has a higher sensitivity at 0% strain. When the sensor with a thicker top electrode (i.e., 110 μm or 210 μm) is stretched to 50%, the top electrode becomes significantly thinner, resulting in a remarkably lower "coverage effect". Therefore, the sensitivity of stretched sensors decreases.

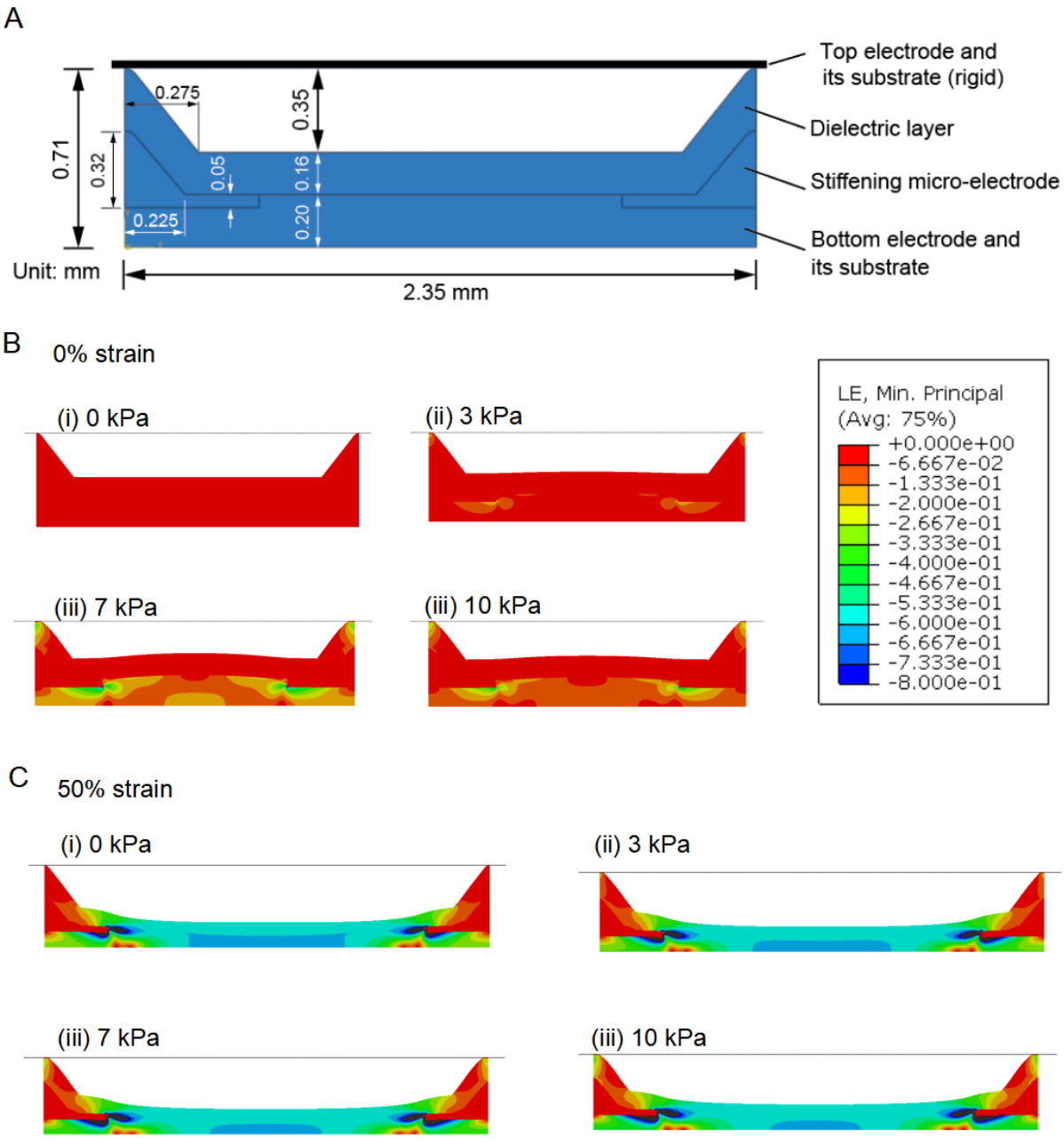

Fig. S1. Finite-element simulations of the stretchable pressure sensor at 0% and 50% strains. (**A**) Dimensions of the model of the sensor. The distribution of the minimum principal logarithmic strain in the lower part of the sensor at 0% (**B**) and 50% (**C**) strain under different pressures (i.e., 0 kPa, 3 kPa, 7 kPa and 10 kPa).

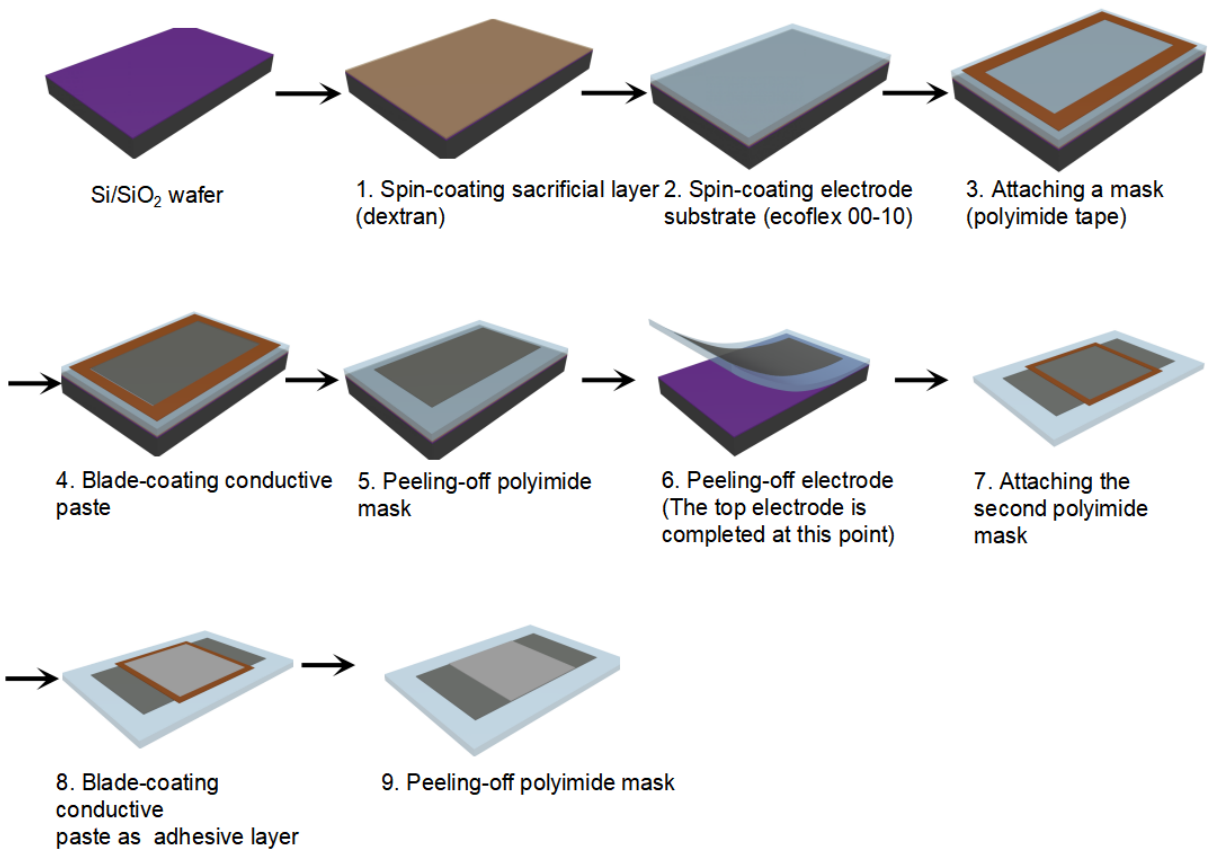

Fig. S2. Fabrication process flow of top electrode (or bottom electrode with adhesive layer).

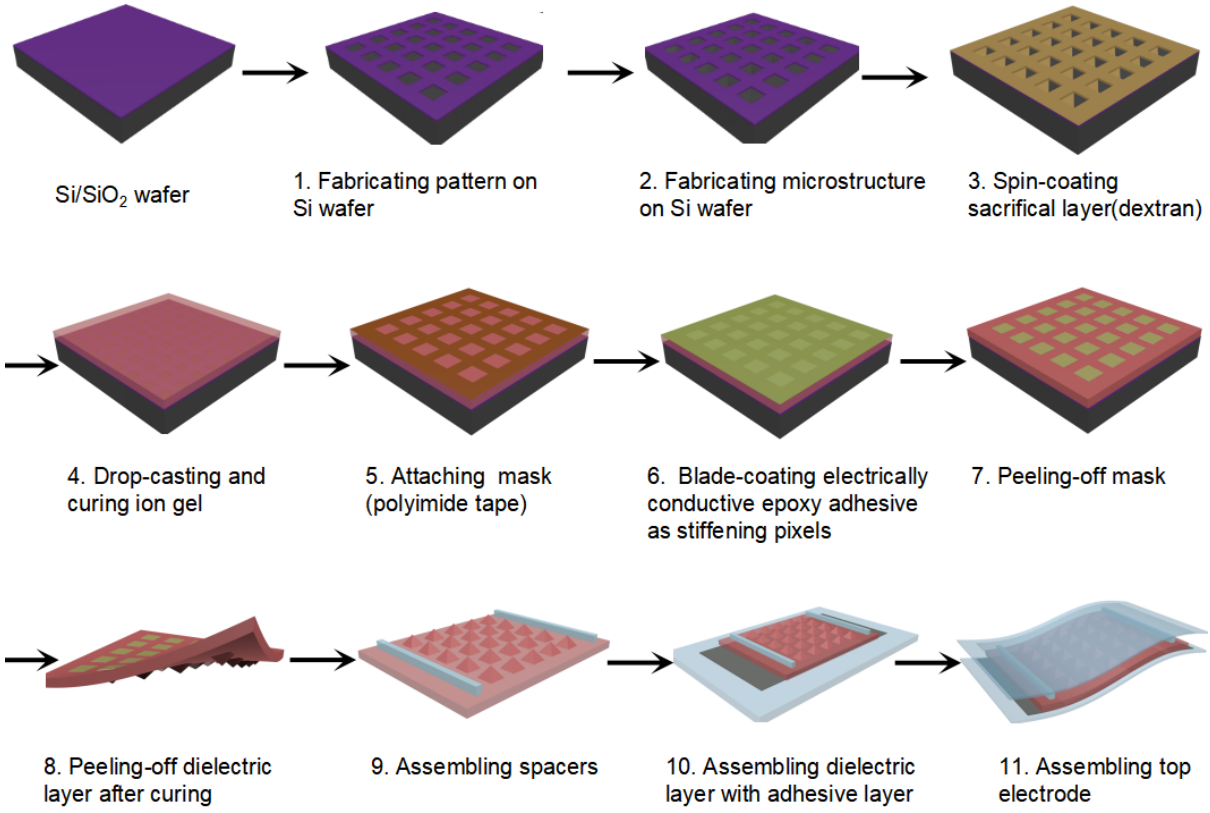

Fig. S3. Fabrication process flow of the stretchable pressure sensor.

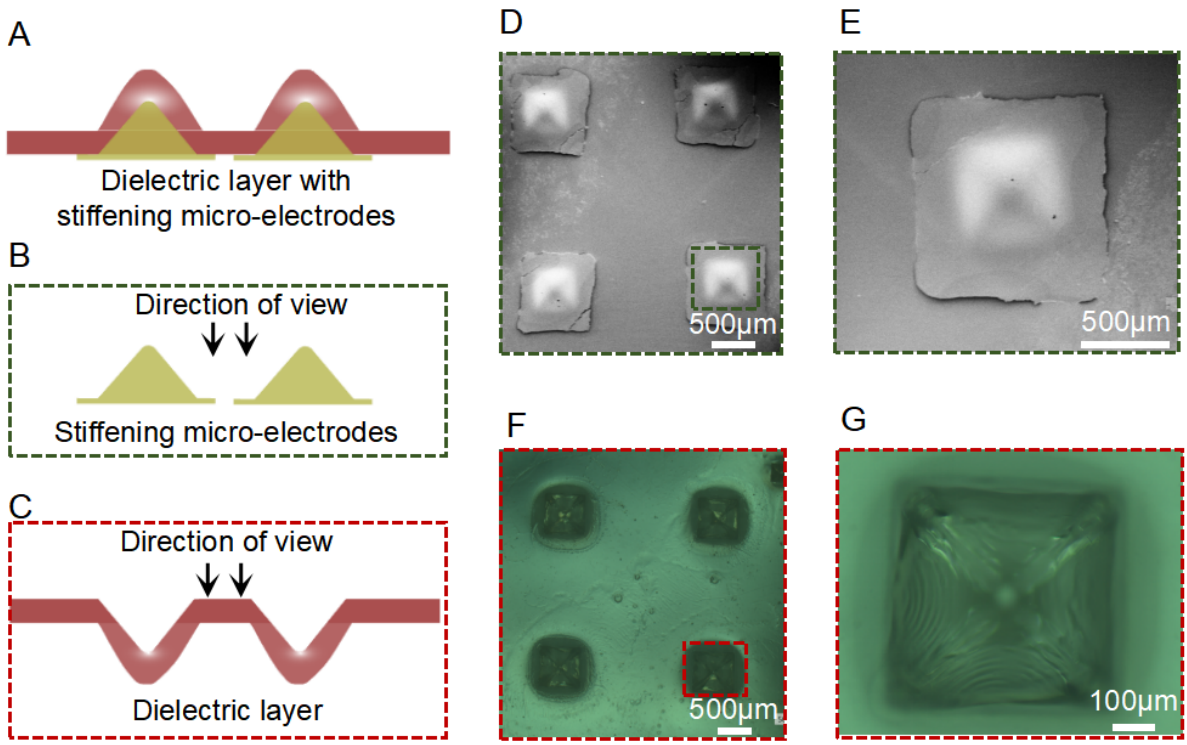

Fig. S4. Schematic, SEM and optical microscopy images of the pyramid structure with stiffened micro-electrodes. (**A**, **B** and **C**) Schematic images of the integrated structure (**A**) of micro-pyramids with stiffened micro-electrodes, stiffened micro-electrodes by themselves (**B**), and micro-pyramids before adding the stiffened micro-electrodes (**C**). (**D** and **E**) SEM images of stiffening micro-electrodes at different magnifications. (**F** and **G**) Optical microscopy image of the reverse side of the micro-pyramid structures, showing the empty volume for further adding the stiffening micro-electrodes.

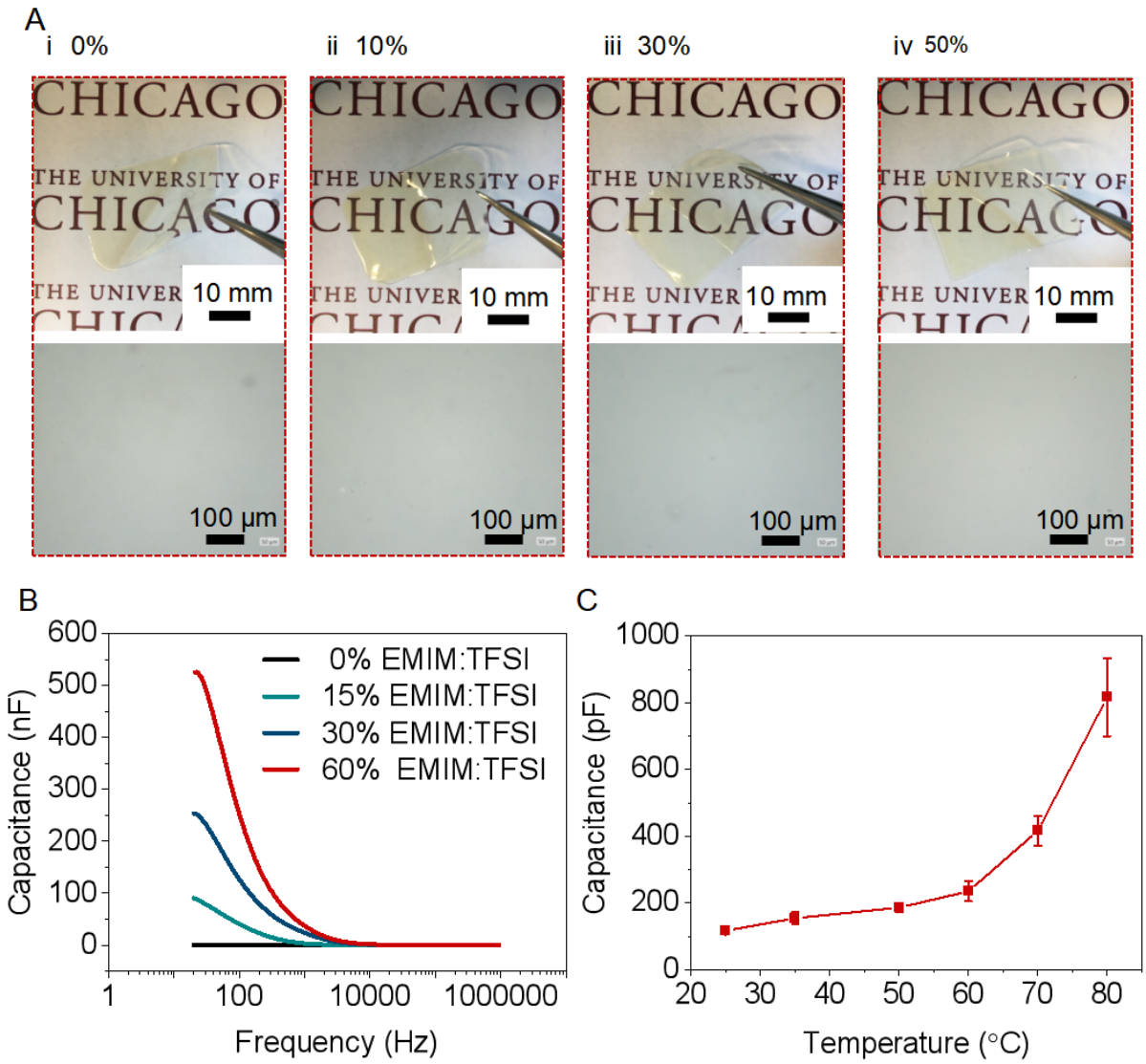

Fig. S5. Characterizations of ionic elastomer films containing variable percentages of EMIM:TFSI. (**A**) Photographs and corresponding microscope images of ionic elastomer films with 1% HMDA and i 0%, ii 10%, iii 30%, and iv 50% EMIM:TFSI. (**B**) Capacitance-frequency relations of the ionic elastomer films containing 1% HMDA and variable percentages of the EMIM:TFSI. Samples were sandwiched between two Ag nanoparticle paste electrodes of 1 cm^2 and the capacitance responses at different frequencies were measured with a LCR meter at 1 V_{rms}. (**C**) The influence of temperature on the capacitance response. The capacitance response was measured with an LCR meter at 1 V_{rms} by applying 4 kPa on the sensor at different temperatures. Photo credit: Qi Su, The University of Chicago.

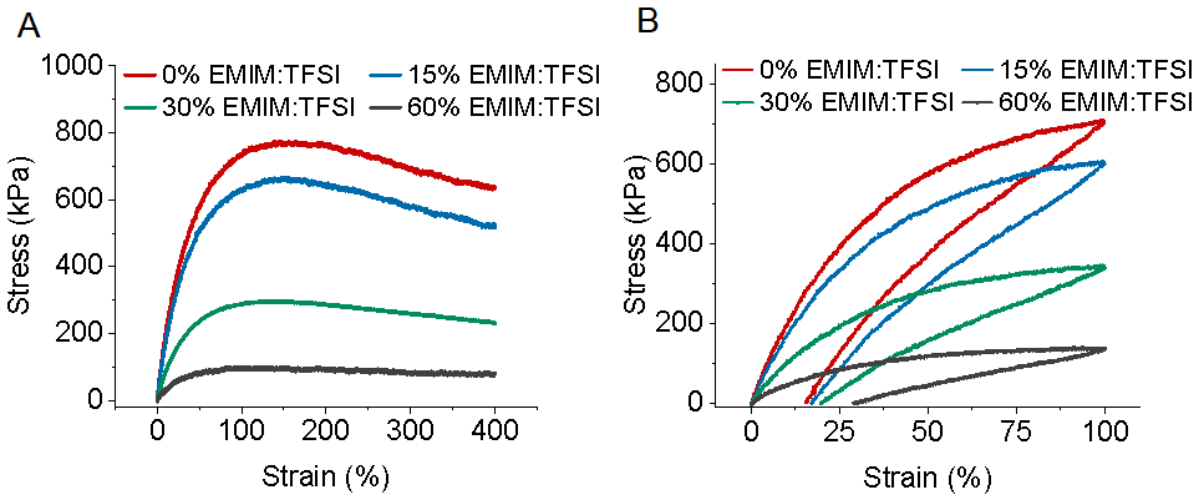

Fig. S6. Mechanical performance of uncrosslinked ionic elastomer films. (**A** and **B**) Stress-strain curve (**A**) and cyclic stress-strain curve (**B**) of uncrosslinked ionic elastomer films containing varied percentages of EMIM:TFSI (i.e., 0%, 15%, 30% and 60%).

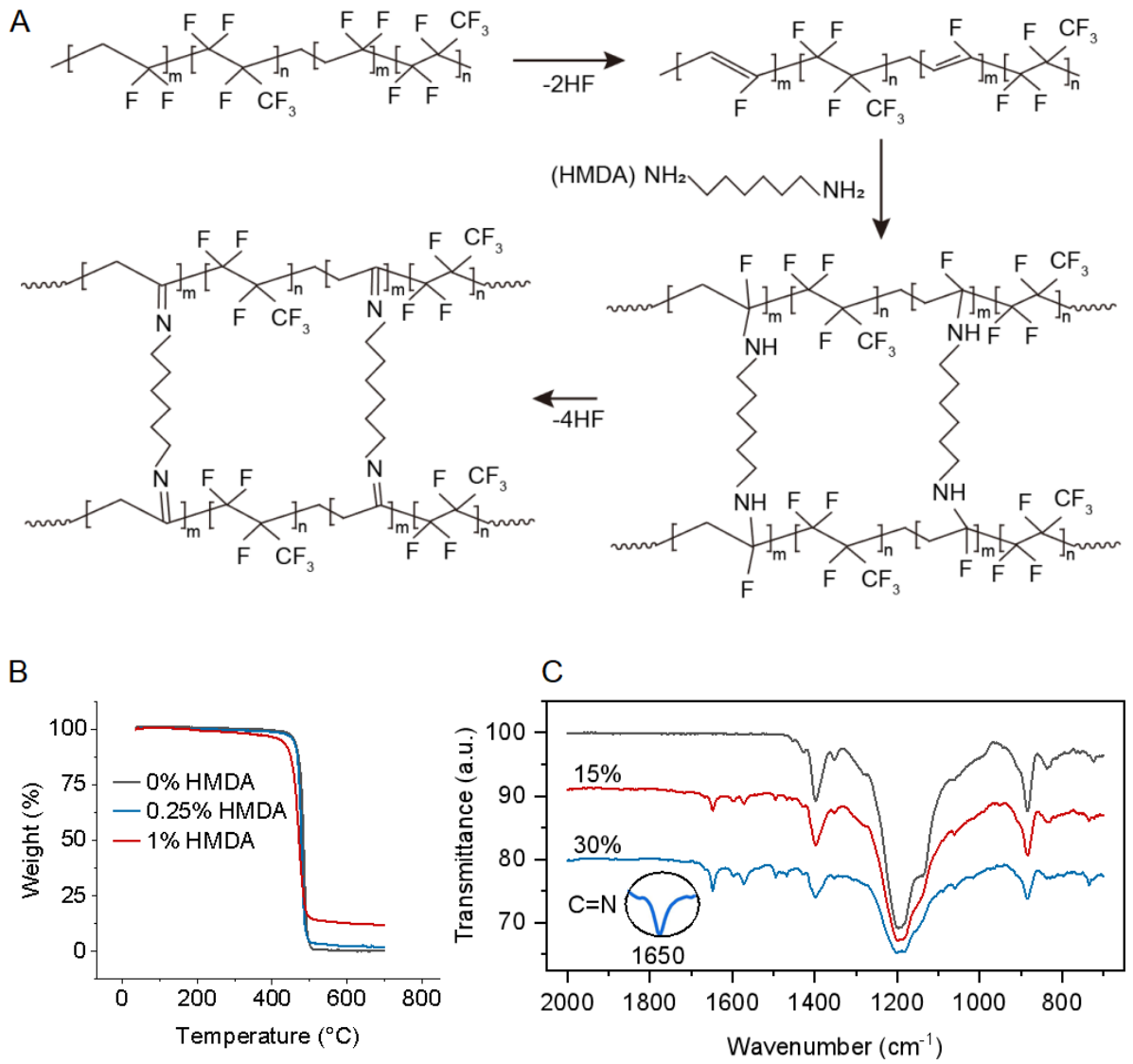

Fig. S7. Mechanism and characterization of crosslinking. (**A**) Schematic diagram of the cross-linking mechanism between PVDF-HFP and HMDA. (**B**) Thermogravimetric curves of pure PVDF-HFP film and PVDF-HFP films cross-linked with 0.25 % and 1% HMDA were measured with TA Instruments Discovery thermogravimetric analyzer (TGA). (**C**) Pure PVDF-HFP film and PVDF-HFP films cross-linked with 15% and 30% HMDA were measured by Shimadzu IRTracer-100; the inset shows the magnified spectrum in the marked region. Absorption peaks at 1201 and 1398 cm^{-1} represent C-F stretching vibration. Additional peaks at 1650 cm^{-1} in the films containing 15% and 30% HDMA represent C=N bonds formed in cross-linking.

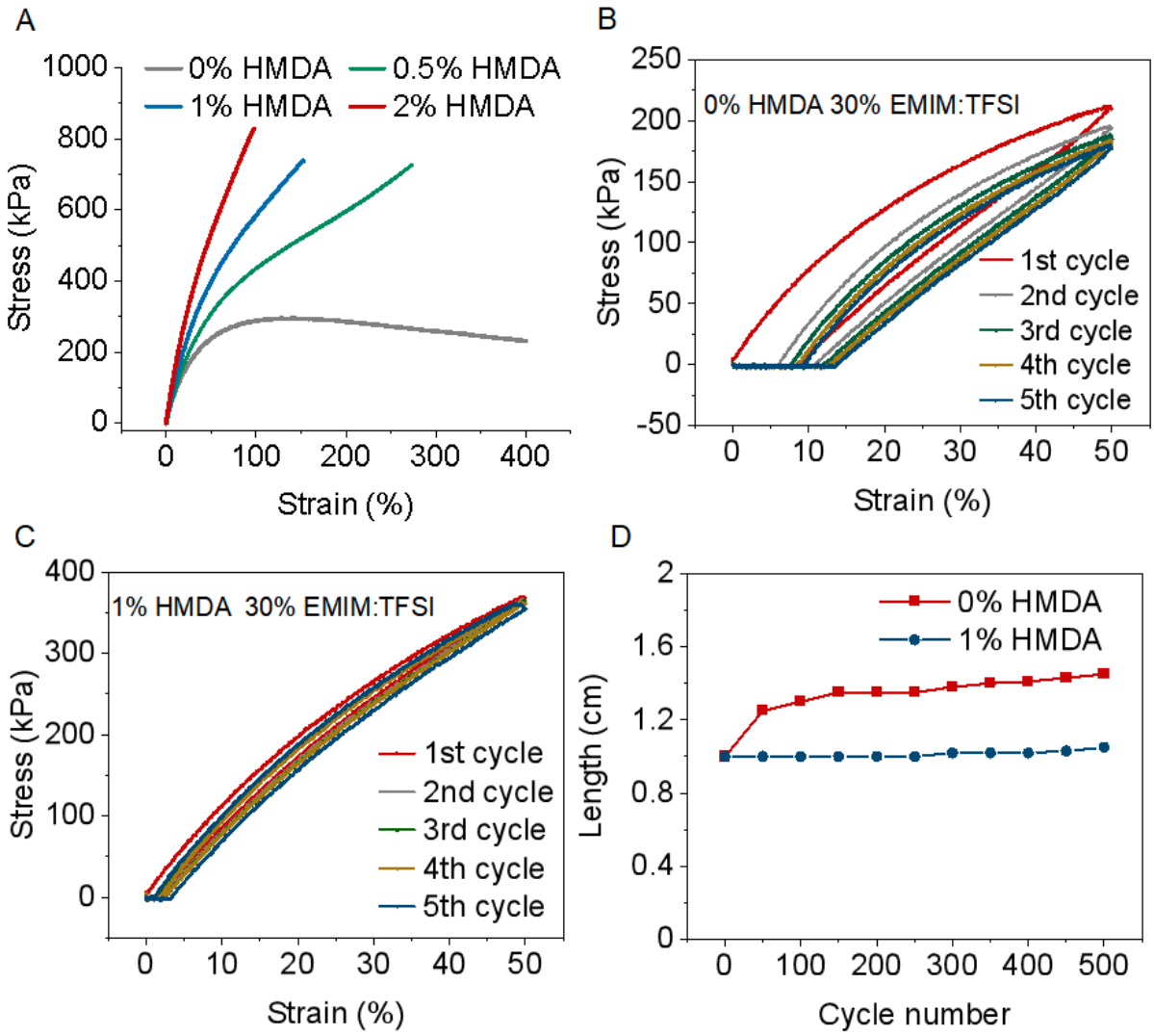

Fig. S8. Elasticity performance of the ionic elastomers. (**A**) Stress-strain curves of the ionic elastomer films all containing 30% EMIM:TFSI but variable percentages of HMDA. (**B** and **C**) Stress-strain curves of repeated cycles of the ionic elastomer films containing 30% EMIM:TFSI and 0% (**B**) and 1% (**C**) HMDA. The maximum strain is 50% for each cycle. (**D**) Fatigue testing of ionic elastomer films containing 30% EMIM:TFSI and varied percentages of HMDA.

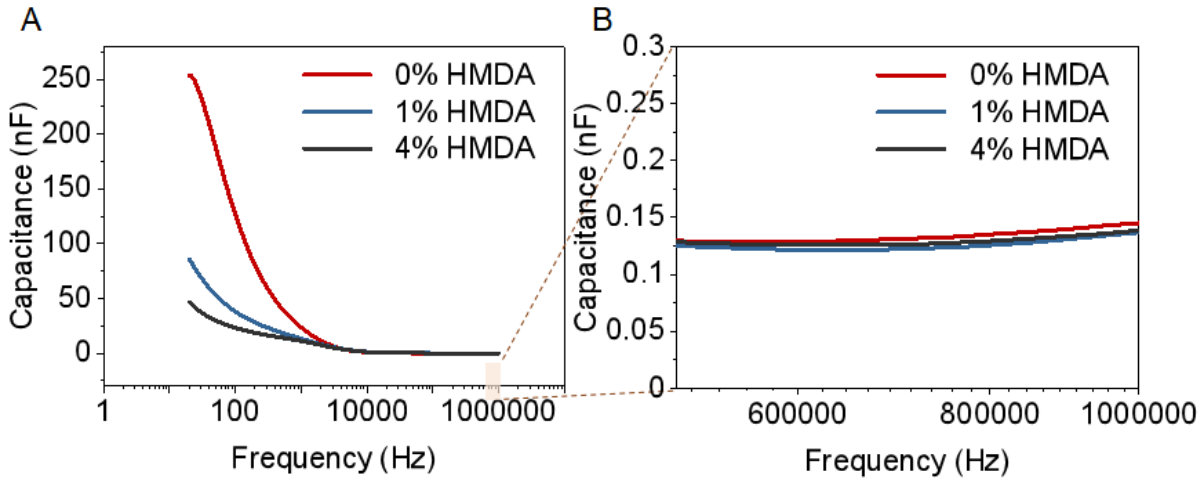

Fig. S9. Capacitances of the ionic-elastomer films at varied testing frequencies. (**A** and **B**) Capacitance-frequency relations of the ionic elastomer films all containing 30% EMIM:TFSI but three different percentages of HMDA (**A**); and the enlarged plot of the high-frequency range (**B**), which is only given by the electrostatic capacitance**.** Samples were sandwiched between two Ag nanoparticle paste electrodes of 1 cm^2 and the capacitances were measured with an LCR meter at 1 V_{rms}.

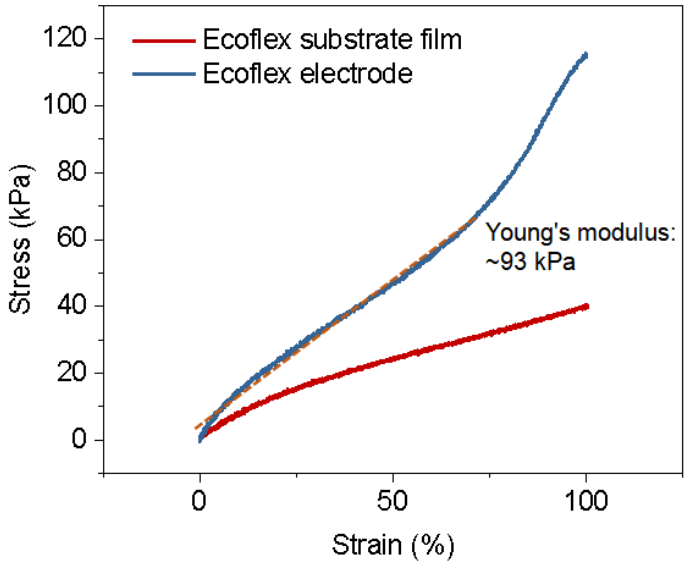

Fig. S10. Stress-strain curve of an Ecoflex substrate film and an electrode. The Young's modulus of the electrode is ~93 kPa.

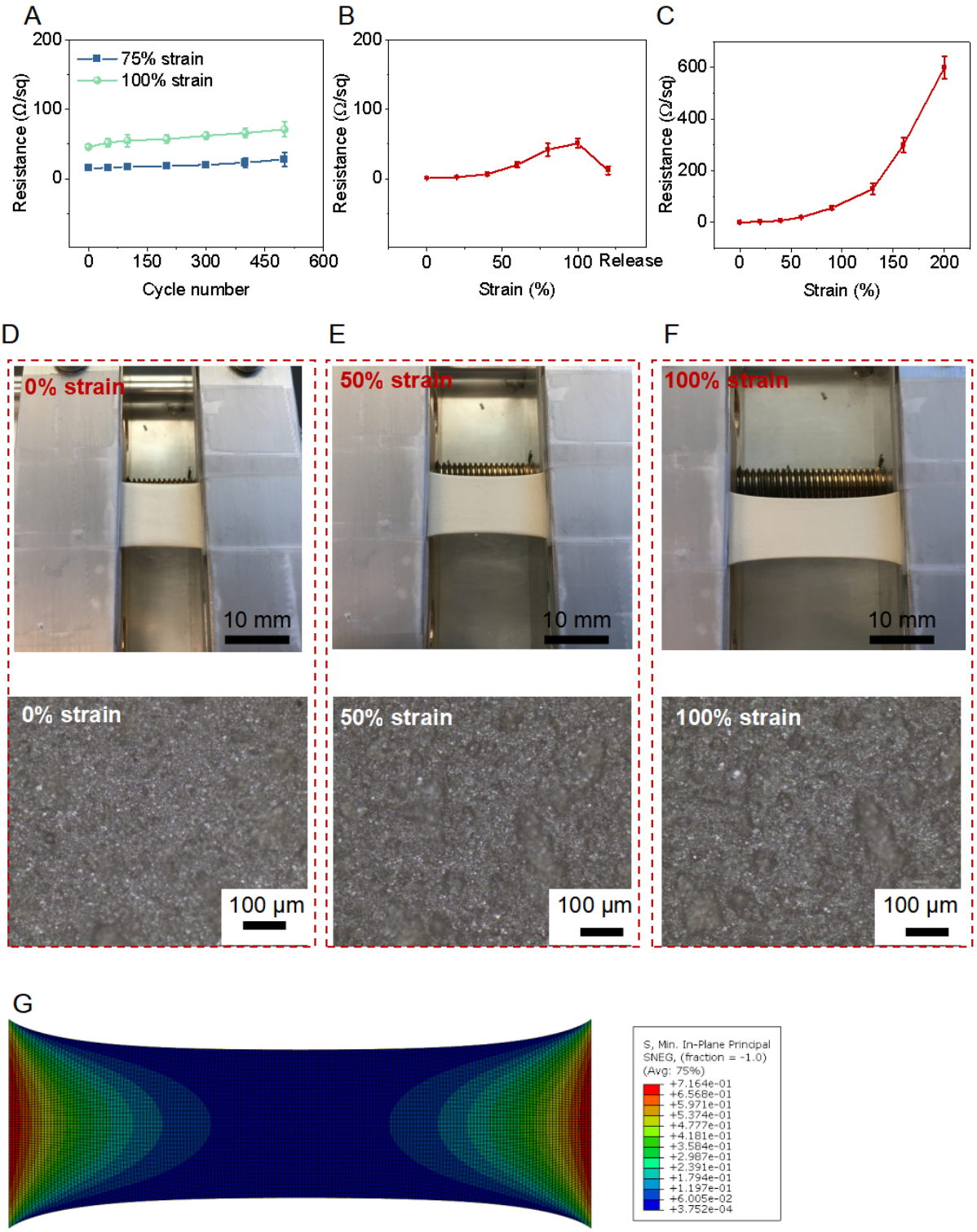

Fig. S11. Characterizations of electrodes. (**A**) Evolvement of the sheet resistance during stretching to 100% strain and after release. (**B**) Evolvement of the sheet resistance of the stretchable Ag-nanoparticle electrode during 500 cycles of repeated stretching to 75% and 100%

strains. The resistances were measured under 75% or 100% strain. (**C**) Influence of stretching on electrode resistance. Error bar was calculated from five electrodes. (**D**, **E** and **F**) Photographs and microscope images of electrodes at 0% (**D**), 50% (**E**) and 100% (**F**) strains. (**G**) The distribution of the minimum in-plane principal stresses when a 100% tensile strain is applied in the longitudinal direction. Photo credit: Qi Su, The University of Chicago.

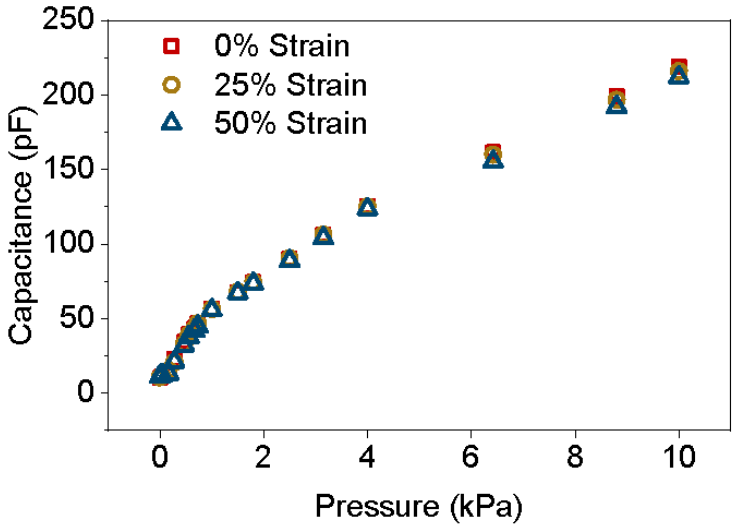

Fig. S12. Capacitance responses of the sensor at 0%, 25% and 50% strains.

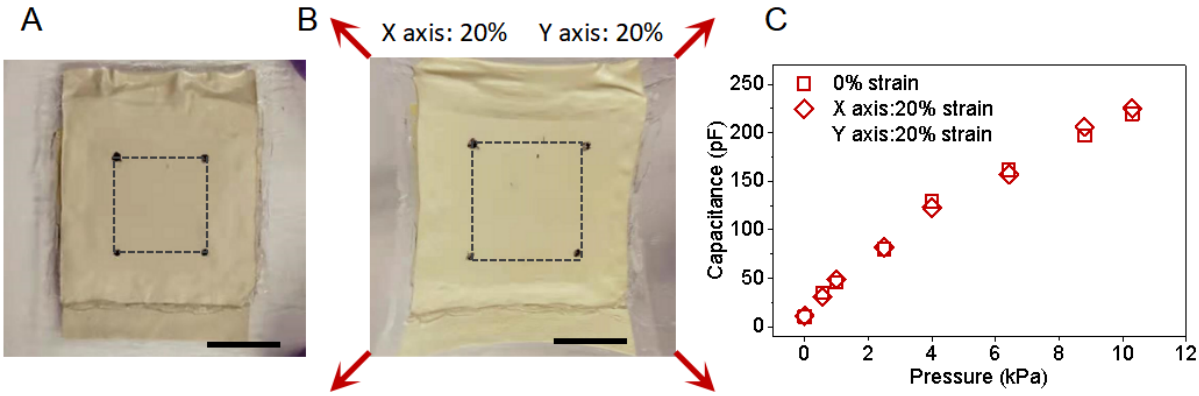

Fig. S13. Biaxial stretching of the sensor. Photographs (**A** and **B**) and capacitance responses (**C**) of the sensor under 0% and 20% strains in two axes. Photo credit: Qi Su, The University of Chicago.

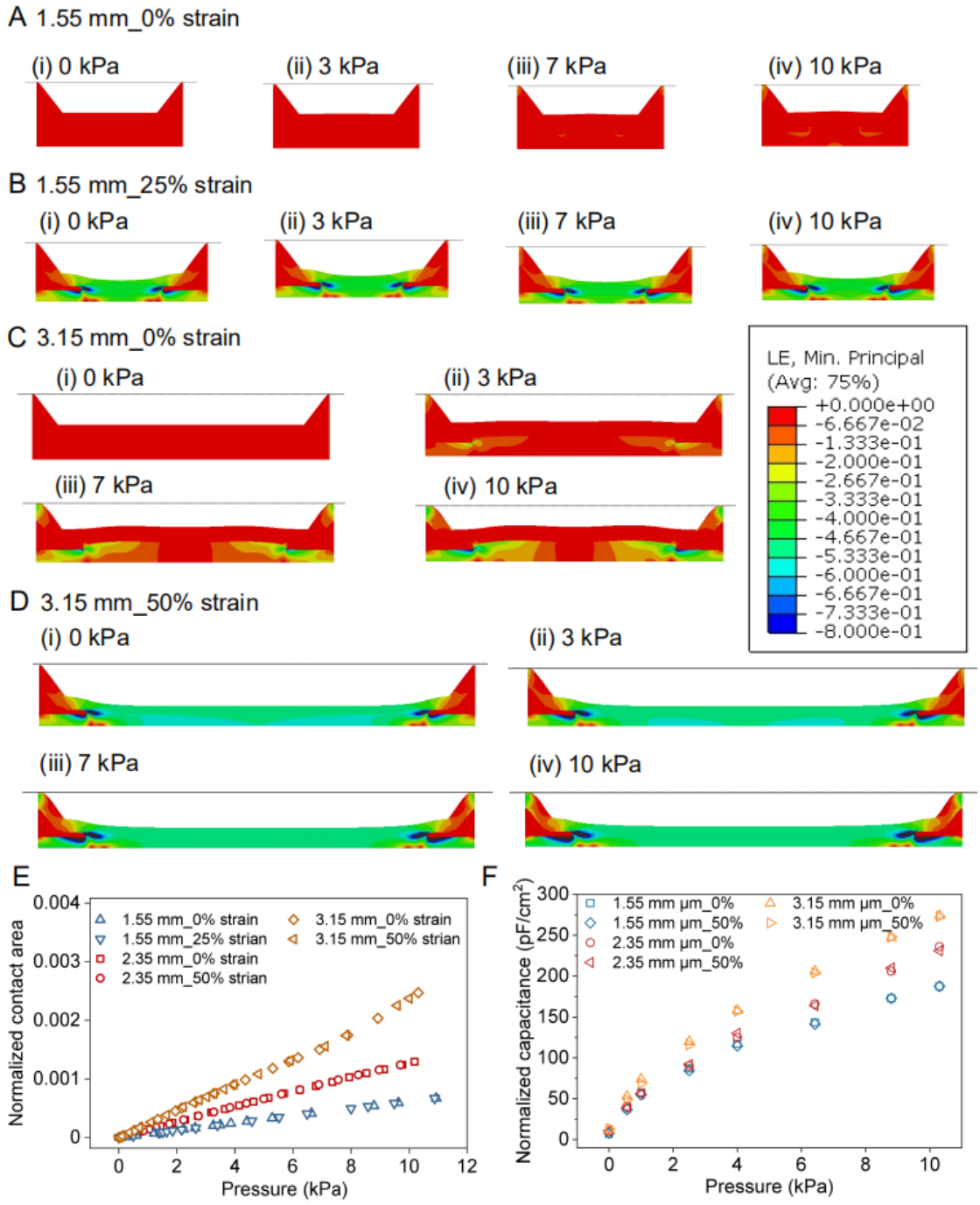

Fig. S14. Comparison of sensors with varied pyramid densities. (**A**, **B**, **C** and **D**) Sensor structures with a smaller (i.e., 1.55 mm) (**A** and **B**) and a larger (i.e., 3.15 mm) (**C** and **D**) interspace distances between adjacent pyramids are modeled and simulated. (**E**) Simulation results of the relation between normalized contact area and applied pressure. (**F**) Experimental results of the relation between normalized capacitance and applied pressure for these sensor structures. The normalizations are made to the total areas of the sensors.

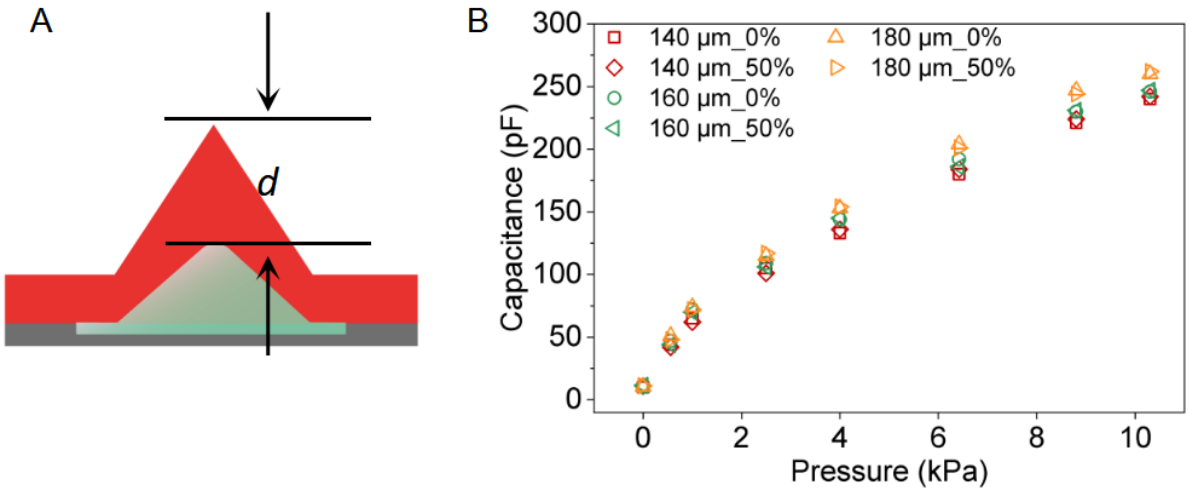

Fig. S15. Capacitance responses of the sensors with the ionic dielectric layer of varied thicknesses. The increase of the dielectric's thickness is accompanied with the increase of the thickness of the ionic elastomer in the pyramid microstructure (i.e. the parameter *d* labeled in **A**), which will make the overall compression stiffness of the pyramid microstructure smaller.

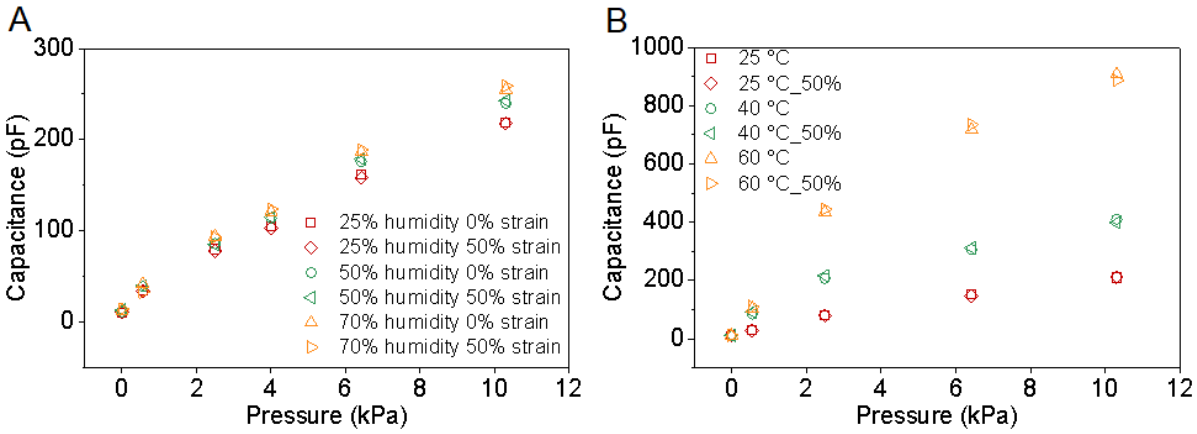

Fig. S16. Pressure sensing performance under varied humidities and temperatures. Influences of humidity (**A**) and temperature (**B**) on the sensor's performance at 0% and 50% strains.

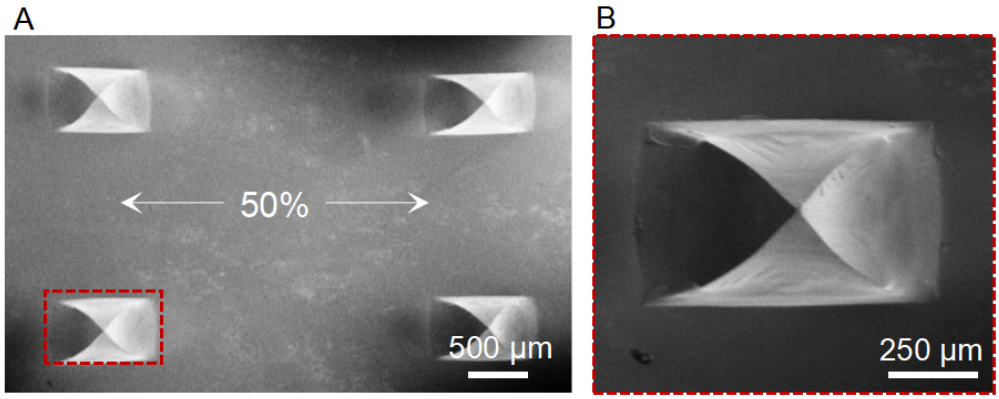

Fig. S17. SEM images of pyramids. Top-view of a dielectric layer (**A**) and enlarged view of a pyramid (**B**) without stiffening pixels at 50% strain.

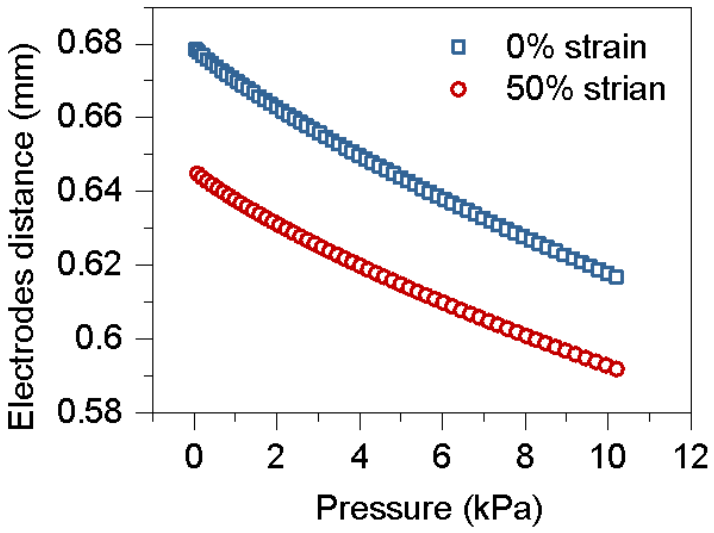

Fig. S18. Simulation results of the distance between the top and bottom electrodes under varied pressures.

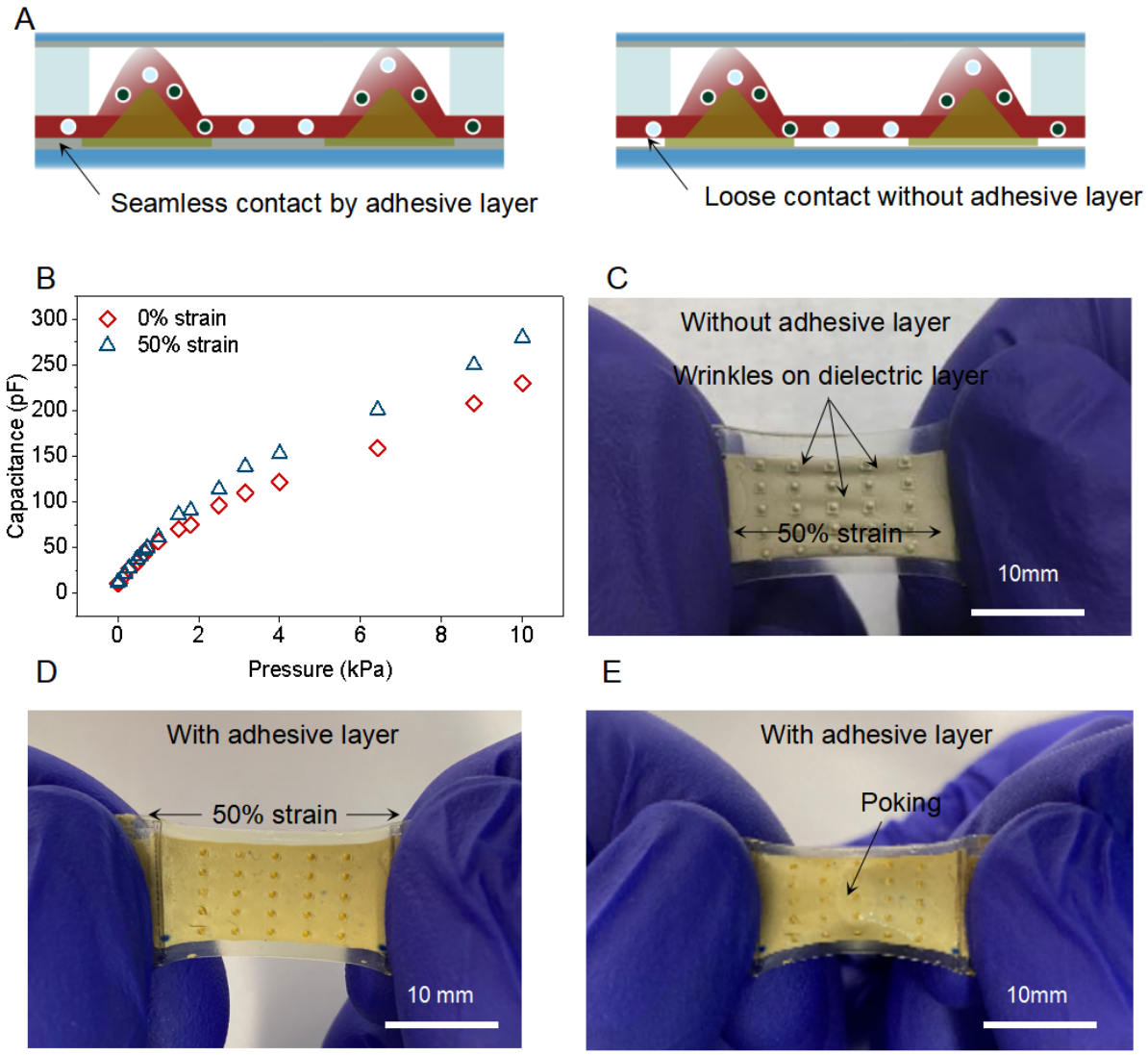

Fig. S19. Characterization of the reference sensor without the adhesive layer. (**A**) Schematic illustrations of our sensor with the adhesive layer (left) and the reference sensor without the adhesive layer (right). (**B**) Capacitance responses of the sensor without the adhesive layer to varied pressures. (**C**) Wrinkles on the dielectric layer when the sensor is stretched to c.a. 50% strain. (**D** and **E**) The sensor with adhesive layer shows intimate contact between the dielectric layer and bottom electrode (**D**) at 50% strain and (**E**) under poking. Photo credit: Qi Su, The University of Chicago.

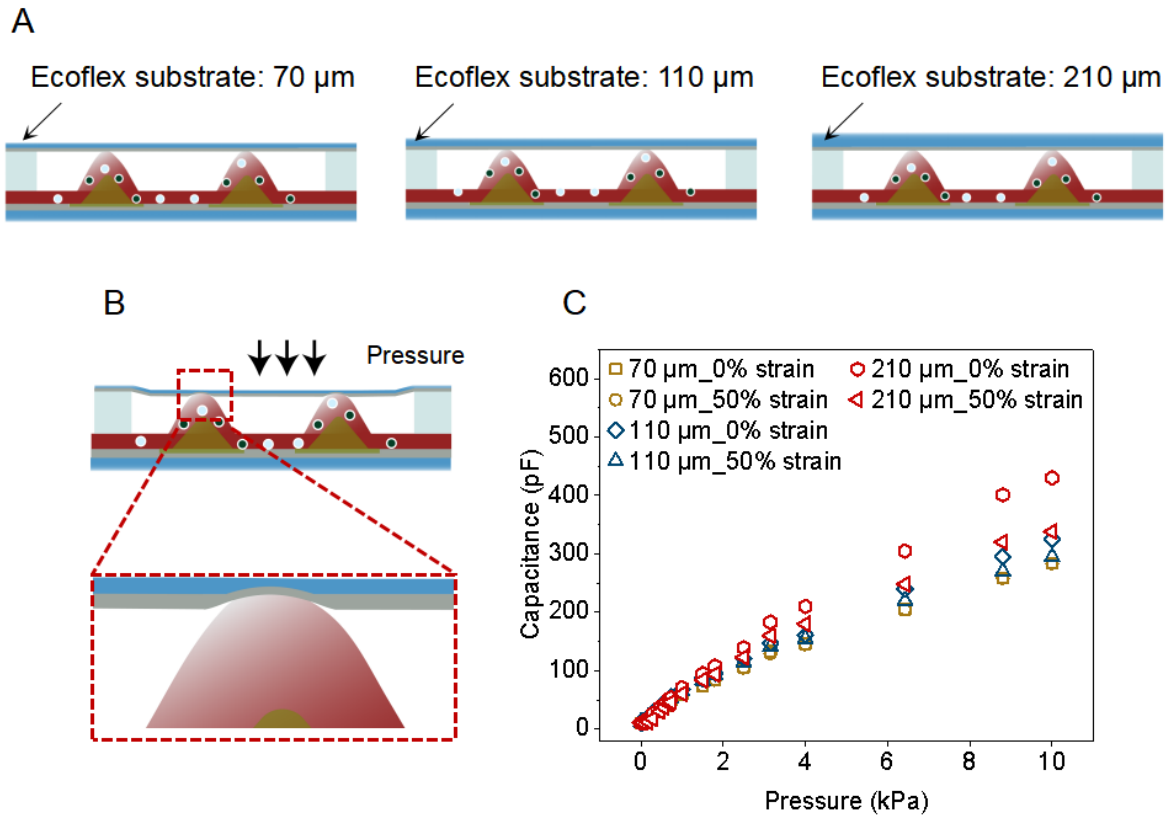

Fig. S20. Characterization of the reference sensor with Ecoflex top-electrode substrates of different thicknesses. (**A**) Schematic illustration of the sensors with Ecoflex top-electrode's substrates of different thicknesses. (**B**) Schematic illustration of "Coverage effect" of top electrodes. (**C**) Capacitance response of the reference sensors.

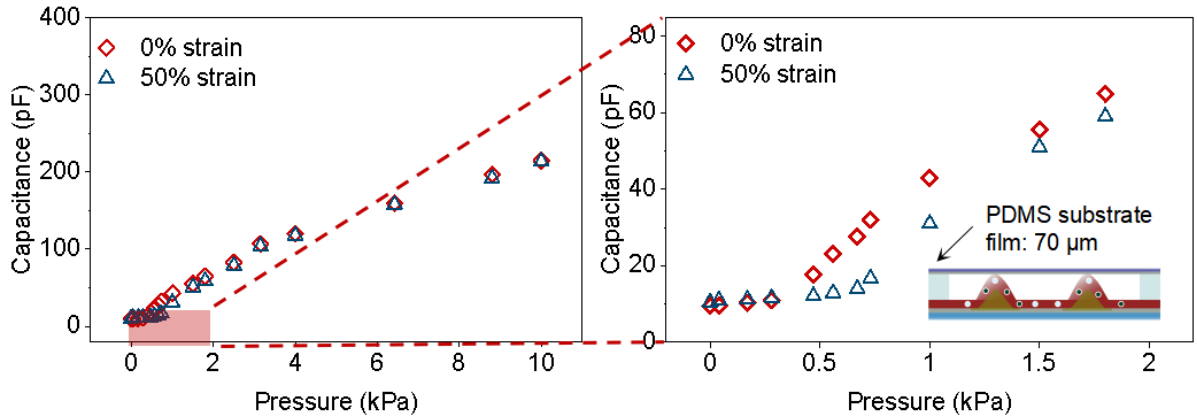

Fig. S21. Characterization of the reference sensor with the PDMS substrate of top electrode.

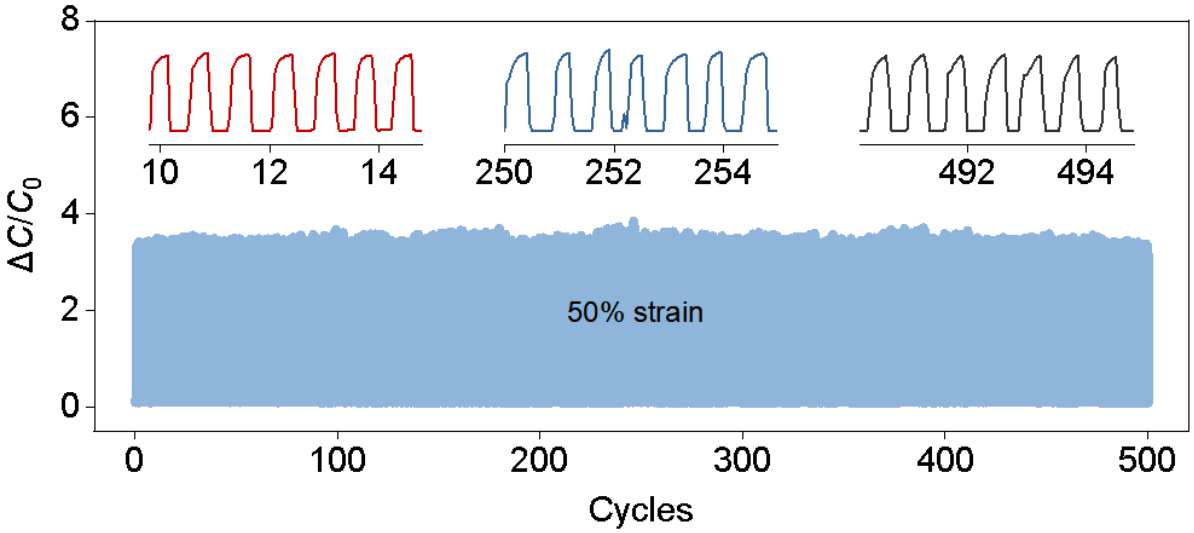

Fig. S22. Fatigue testing of the stretchable pressure sensor at 50% strain. The robustness of the sensor was tested with an applied pressure of 0.67 kPa and 50% strain 500 cycles. The insets display signals from cycles # 10-15, 250-256, and 490-496.

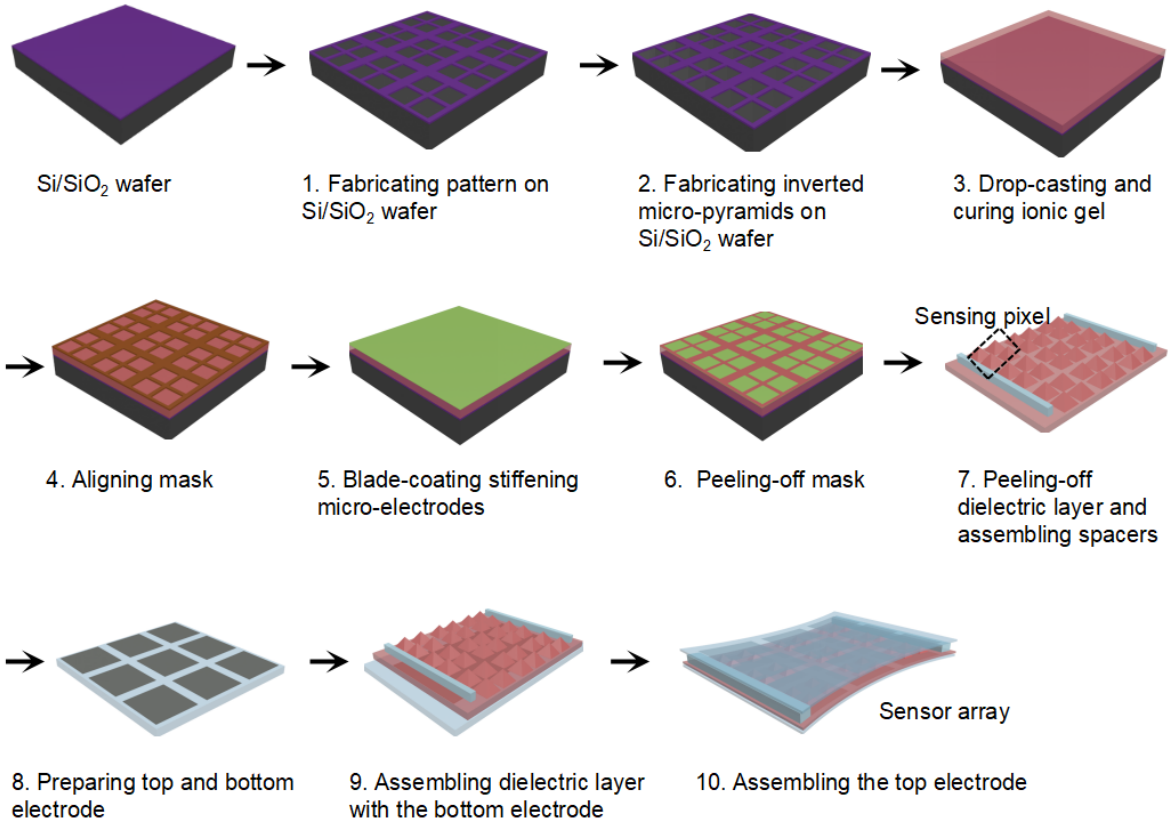

Fig. S23. Fabrication process flow of the stretchable pressure sensor array.

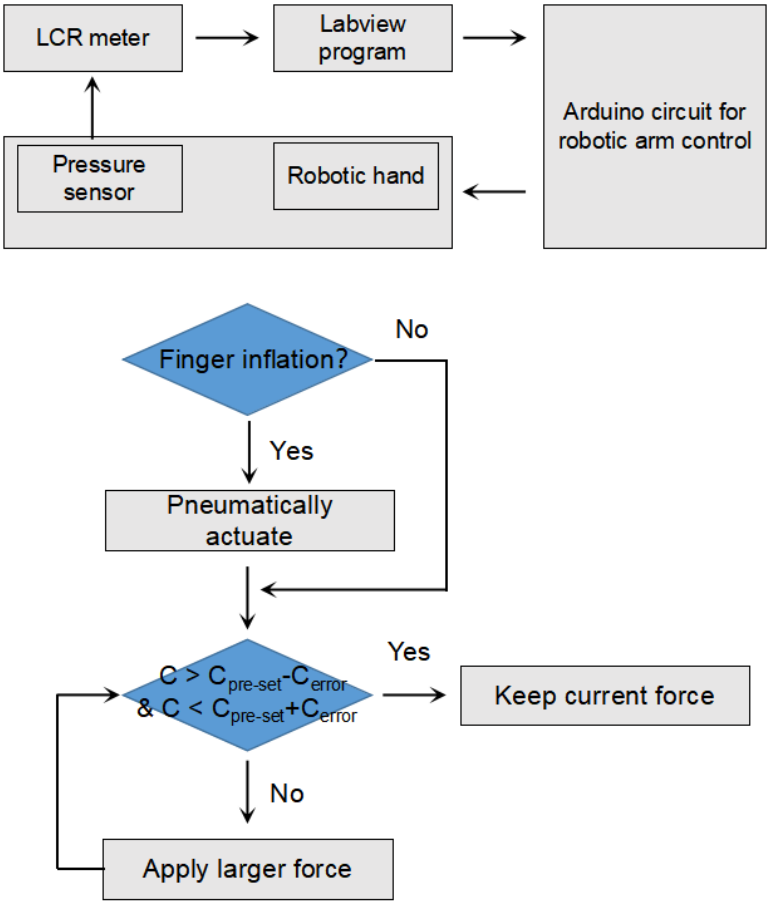

Fig. S24. Logic diagram for the closed loop control of the sensorized robotic hand. The Labview program sends the commands to the Arduino circuit that controls the robotic arm, based on the pressure feedback measured by the pressure sensor on the robotic hand. C is the current capacitance of the stretchable sensor, $C_{pre\text{-}set}$ is the pre-set capacitance value, C_{error} is the error range of pre-set capacitance value.

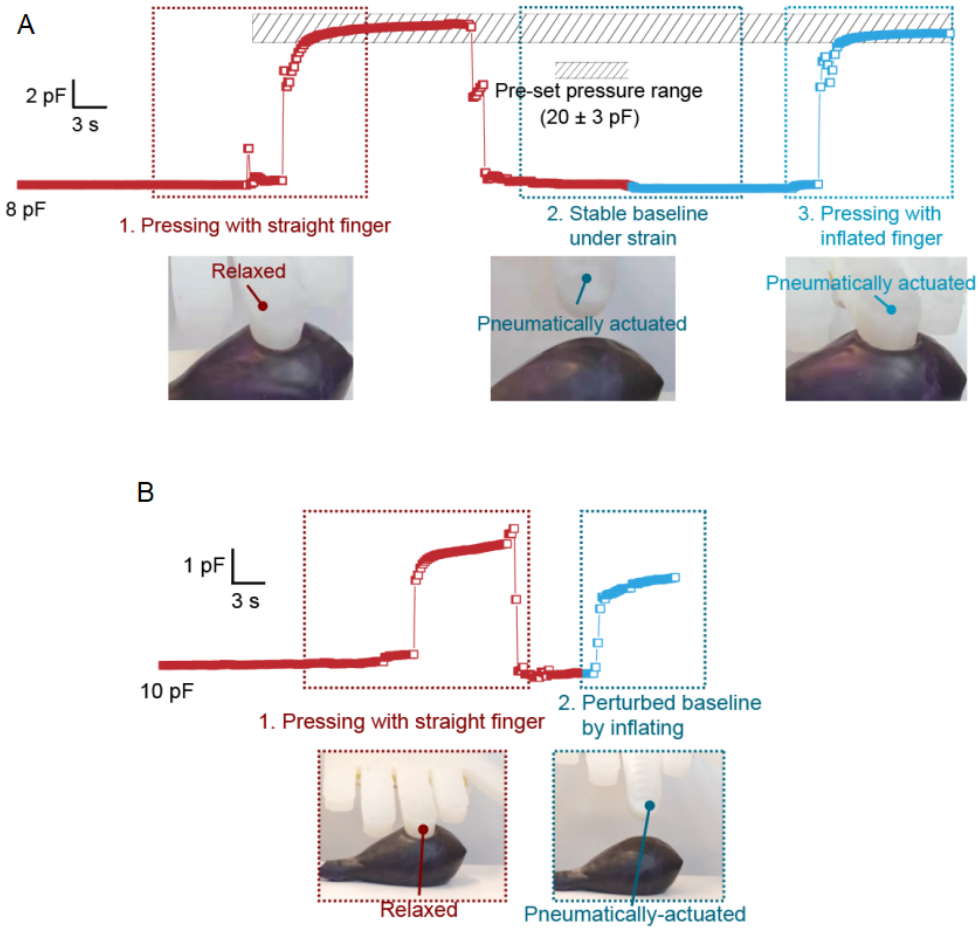

Fig. S25. Use of our strain-unperturbed stretchable pressure sensor, and also a conventional stretchable pressure sensor as a comparison, for applying very gentle touch on a very soft surface. (**A**) Real-time capacitance reading from the pressure sensor integrated on a soft-robotic fingertip, which enables the closed-loop control of its attached robotic arm for quantitatively applying a pre-set pressure to a soft object, with the robotic finger changed from the relaxed state to the pneumatically actuated state. (**B**) Real-time capacitance reading from a conventional stretchable sensor. The capacitance shifts significantly when the soft robotic finger is pneumatically actuated. Photo credit: Sihong Wang, Qi Su, The University of Chicago.

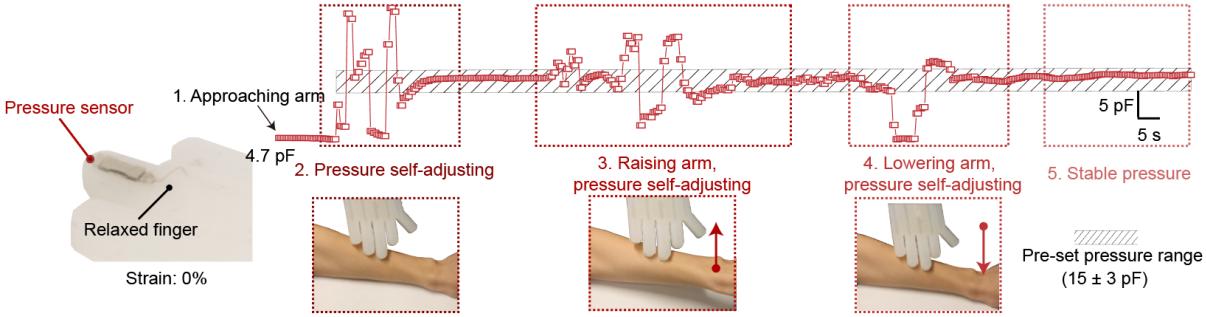

Fig. S26. Use of the stretchable pressure sensor on a soft-robotic fingertip in the undeformed state for applying pressure on a human arm. Real-time capacitance reading from the pressure sensor integrated on a soft-robotic fingertip, which enables the closed-loop control of its attached robotic arm for applying and self-adjusting a force, with a pre-set pressure value, onto the top surface of a human arm. Photo credit: Sihong Wang, Qi Su, The University of Chicago.

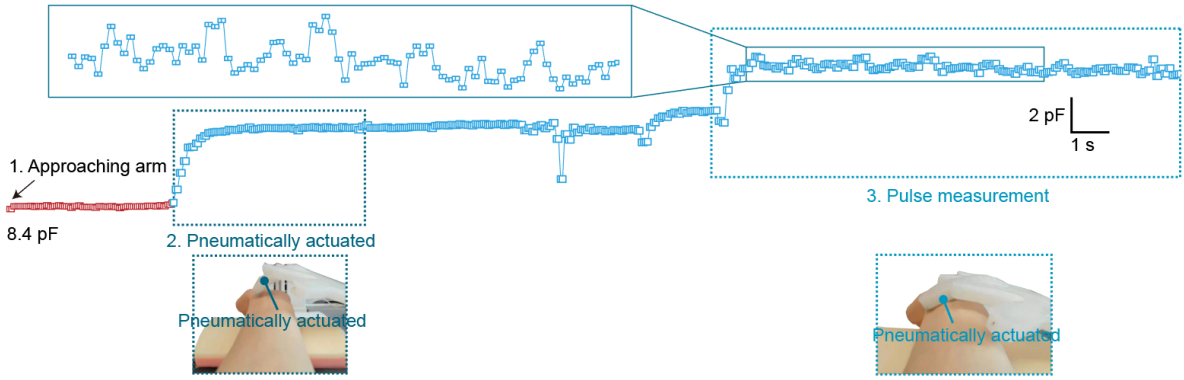

Fig. S27. Use of a conventional stretchable pressure sensor for pulse measurement. The capacitance shifts significantly and cannot measure pulse signal with high signal-to-noise ratio when the soft robotic finger is pneumatically actuated. Photo credit: Sihong Wang, Qi Su, The University of Chicago.

Table S1. Comparison of our stretchable pressure sensor with previous works of stretchable pressure sensors.

	Capacitive				Resistive		
Ref.	This work	(*28*)	(*30*)	(*31*)	(*25*)	(*26*)	(*34*)
Top electrode	Ag paste/Ecoflex	Silver nanowire/ Polyester yarn	Deep eutectic solvent gel electrolytes	Mg/Polylactic acid	Conductive Fabric	N/A	Pt/PMDS
Bottom electrode	Ag paste/Ecoflex	Silver nanowire/ Polyester yarn	Deep eutectic solvent gel electrolytes	Mg/Polylactic acid	PEDOT:PSS/ Polyurethane	PEDOT:PSS/SWCNT	Pt/PMDS
Dielectric layer	PVDF/EMIM:TFSI/ HMDA ionic elastomer	PDMS/Dragon skin /Ecoflex	VHB tape	Poly(glycerol sebacate)	N/A	N/A	N/A
Sensitivity (kPa^{-1})	4.5 (0-1 kPa) 2.0 (1-10 kPa)	0.012	0.0125	0.13	2	0.005	0.13
Detection of limit (Pa)	0.2	1.5	c.a. 100	12	23	28	5
Strain-insensitivity	~98%	~0%	~20%	~0%	~62%	~65%	~30%
Working strain	50%	40%	125%	15%	40%	30%	4%
Response time of loading (ms)	50	31	c.a.307	c.a. 150	200	c.a. 62	50
Pressure sensing range (kPa)	0 - 10	0 - 50	0 - 160	0 - 10	0 - 8	0 - 40	0 - 1.5
Compression robustness (times)	>500	10000	N/A	30000	N/A	N/A	N/A
Linearity (R^2) (0-10 kPa)	0.98	0.95	0.99	0.99	0.98	0.82	0.95